Effect of chordwise deformation on unsteady aerodynamic mechanisms in hovering flapping flight

T. A. Noyon[1]*, W. B. Tay[1,2], B. W. van Oudheusden[1], and H. Bijl[1]
1. Delft University of Technology, Delft, The Netherlands
2. Temasek Laboratories, National University of Singapore, Singapore

ABSTRACT

A three-dimensional simulation of hovering flapping wings was performed using an immersed boundary method. This was done to investigate the effects of chordwise wing deformation on three important unsteady aerodynamic mechanisms found in flapping flight, namely Leading Edge Vortex (LEV) shedding, wake capture and clap and fling. A wing was modeled as a flat plate, flapping close to a symmetry plane. Three different deforming chords were defined, a rigid case, a case with maximum deformation at the trailing edge and increased angle of attack (AoA) near the leading edge, and a case with the maximum deformation in the center of the chord and decreased AoA near the leading edge. All cases had zero deformation at the wing root and maximal deformation at the wing tip. A higher AoA near the leading edge resulted in faster LEV buildup and faster buildup of lift. No shedding of the LEV was observed in any of the cases even when deformation caused a high AoA near the leading edge. A distinct dip in lift buildup was observed and shown to be caused by the interaction between the previously shed vortex and the newly developing LEV. This interaction occurred faster when the AoA at the leading edge was increased, and slower when the angle of attack was decreased. Moving the wing closer to the symmetry plane had a positive effect on the cycle average value of C_L. This positive effect was reduced however by the earlier interaction between the LEV and the previously shed vortex.

1 INTRODUCTION

In view of the Reynolds number range at which MAVs operate and the desired flight performance flapping flight concepts are considered beneficial, since fixed-wing aircraft do not have the desired maneuverability and helicopters are too inefficient and noisy [1]. This has motivated designers to look to nature for inspiration, since insects are extremely maneuverable, silent and can be more efficient at low flight speeds [2]. The aerodynamics of insect flight are very different from those of fixed wing aircraft or rotorcraft however, since it exploits unsteady aerodynamic mechanisms to generate sufficient lift force, including a stable leading-edge vortex (LEV), clap and fling use of rotational mechanisms and wake capture [3]. Biologist have been interested in the flying capabilities of insects for a long time and have conducted many experiments using free flying insects [3], tethered insects [4] and dynamically scaled mechanical flappers [4, 5, 6]. To further understand the effect of all relevant parameters it is essential to quantify and visualize the three-dimensional flow around the wings. Although recent developments in non-intrusive measurement techniques allow researchers to capture three dimensional flow fields [7, 8], it remains very difficult to capture all relevant details of the flow using only experimental techniques. Therefore numerical simulations can provide additional information for understanding the flow phenomena [9]. Several three-dimensional simulations have been performed on specific insect geometries, however, the computational requirements of such simulations are too demanding to do a systematic parametric study of all the important parameters involved. More general studies on the wing flexibility have used two-dimensional simulations and have particularly noted the positive effect of a more flexible wing on leading edge vortex (LEV) stability [10, 11, 12], which in turn has a large positive effect on the lift force. The LEV stability is also affected by three dimensional flow however [13, 14], so the benefit of a flexible wing in a three dimensional case cannot be determined from a two-dimensional simulation alone. Studies investigating the three-dimensional effects in flapping flight using simulations with rigid wings have shown that the tip vortex created at the free end of the wing stabilizes the LEV, from which can be concluded that this stability is also affected by the aspect ratio of the wing [15] and the kinematics of the wing [16]. To get a complete picture of how different parameters affect the LEV stability, and with that the force coefficients of the wing, a three-dimensional simulation is required.

The objective of the present study is to perform a three-dimensional simulation of hovering flapping wings, in order to investigate the effects of chordwise wing deformation on three important unsteady aerodynamic mechanisms found in flapping flight, namely LEV shedding, wake capture and clap and fling. This will result in a better understanding of the physics involved in flapping flight, which in turn could lead to

*Email address(es): tijsnoyon@gmail.com

improved MAV designs. Since the actual three-dimensional deformation of both insect and MAV wings is very specific to the wings' structural and material properties, this study does not attempt to include fluid-structure interaction, instead prescribing the time dependent deformation of the wings directly. The direct prescription of the wing deformation allows a more controlled way to investigate its effect on the unsteady aerodynamic mechanisms. The configuration of the wings that will be simulated is based on a wing pair as found on a four-winged MAV in biplane configuration such as the DelFly [17]. This means the wings will rotate in opposing phase around a point at the leading edge root. Under this condition the flow around one wing will be affected by the presence of the other wing. The wing interaction effects will be modeled by creating a symmetry plane, and investigated by varying the distances to the symmetry plane. Only deformation in chordwise direction will be investigated in this study, with the wing considered fully rigid in spanwise direction. However, the chordwise deformation will be varied along the span, resulting in a twist in spanwise direction.

2 Numerical Method

A serious issue in simulating flapping wings is the large translational and rotational motions of the wings. In conventional body conforming grid simulation methods these large movements result in large grid deformations, which causes problems in convergence and stability of the algorithms as well as having a negative impact on the accuracy [18]. The Immersed Boundary Method (IBM) used in this study is a combination of the methods described by [19], [20] and [21]. In both the method by [21] and the one by [20] the forcing term fc is calculated explicitly using an Adam-Bashforth second-order (AB2) scheme. In this study, fc is calculated explicitly using the first-order forward Euler and second-order AB2 schemes for the viscous and convective terms, respectively. This will reduce the computational cost while having no observable difference on the results compared to an AB2 scheme [22]. The forcing term fc will be calculated according to Equation 1.

$$fc^{n+1} = \frac{u_f - u^n}{\Delta t} + \left[u^n \cdot \nabla u^n - \frac{1}{\mathcal{R}e} \nabla^2 u^n \right] + \nabla p^n \quad (1)$$

In this equation the superscript indicates the time step number and u_f is the velocity contribution of the boundary which has to be imposed. Since the boundary does not match the grid this velocity is not known and is obtained through a simple triangle linear interpolation of the interface and three points in the surrounding velocity field [22]. Finally the total force exerted on the surface of the solid will be calculated using fc^{n+1}, according to Equation 2.

$$F_i = -\int_{solid} fc_i^{n+1} dV + \int_{solid} \left(\frac{\partial u_i}{\partial t} + \frac{\partial u_i u_j}{\partial x_j} \right) dV \quad (2)$$

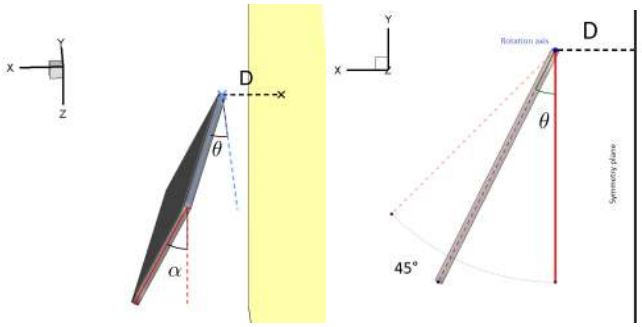

Figure 1: Three-dimensional view of the flapping motion.

This method displays spurious pressure fluctuations due to its method of dealing with the immersed boundary [23]. To reduce the effect of these fluctuations on the results, the force response of several flapping cycles will be averaged.

3 Simulation Setup

To investigate how deformation of the chord affects the aerodynamic mechanisms around a flapping wing under hovering conditions, a simplified wing model has been created for the flow simulations. A wing will be modeled as a rectangular flat plate with a chord of $c = 0.1$[m], a thickness of 0.006[m] and an aspect ratio $AR = 2$. This aspect ratio value is at the lower side of the range of that of flying insects which is between 2 and 10 [24]. Instead of modeling two separate plates, a symmetry plane is used to reduce the required computational resources. Perspective and top views of the wing and the parameters defining the motion are shown in Figure 1. In this figure **D** represents the distance to the symmetry plane, and θ the flapping angle. Insects have a wide range of flapping angles [24] and in this case a total flapping angle θ of 45° is chosen. This flapping angle would be small for two-winged insects but is more typical to that of a four-winged MAV in biplane configuration [17]. The configuration would then correspond to one wing pair, with the assumption that the opposite wing pairs do not influence one another. The motion will start with an outstroke, which results in θ given by Equation 3.

$$\theta = 22.5 - 22.5\cos(ft) \quad (3)$$

Where f is the flapping frequency and t is the elapsed time. The Reynolds number based on the average tip velocity and standard conditions at sea level is equal to $\mathcal{R}e = 2002$, and a reduced frequency of $k = fc/U = 0.319$. All variables are summarized in Table 1. This table also includes the non-dimensionalized variables, which are calculated using the chord length and the average tip velocity. The different deformation scenarios considered in the simulations are detailed in the following subsections.

Parameter	Value	Dimensionless value
Chord	0.1[m]	1
Thickness	0.006[m]	0.06
Aspect ratio	2	2
Average tip velocity	0.314 [m/s]	1
Frequency	1 $[s^{-1}]$	0.319
Reynolds number	2002	2002
Max flapping angle	45°	

Table 1: Parameters of the simulations

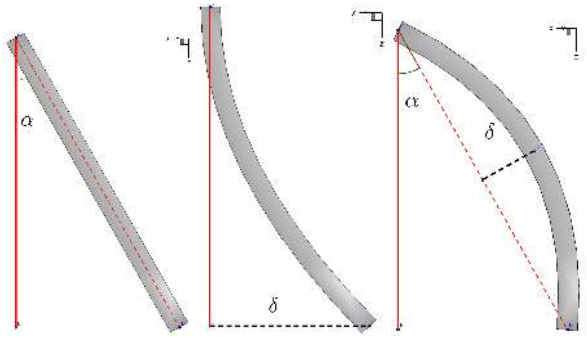

(a) (b) (c)

Figure 2: Chordwise plate deformation profiles. a) Rigid case; b) Deforming end case; c) Deforming center case

3.1 *Rigid case with rotation*

For the rigid plate case the flapping motion described in the previous section is combined with a pitching motion to create an angle of attack. This is done by rotating the plate around the leading edge as shown in Figure 2a. This rotation angle is given by Equation 4.

$$\alpha = -\alpha_{max} \sin(kT) \tag{4}$$

In which α_{max} represents the maximum angle. Note that this angle α is not the angle of attack as conventionally defined, but instead 90 degree minus the angle of attack.

3.2 *Deforming end*

The first deforming case does not contain any pitching, instead an angle of attack is created by the deformation alone. This is achieved by modeling that the leading edge remains straight and the maximum deformation occurs at the trailing edge. The shape of the chord is described using a quadratic function of the distance from the leading edge. The deformation is given by Equation 5.

$$\delta_{end} = -D_{end}^{max} \left(\frac{z}{c}\right)^2 \sin(kT) \tag{5}$$

Where D_{end}^{max} is the maximum deformation and $\frac{z}{c}$ is the distance from the leading edge normalized by the length of the chord. The resulting shape is shown in Figure 2b. It can be seen that this shape increases the angle of attack near the leading edge compared to the rigid case.

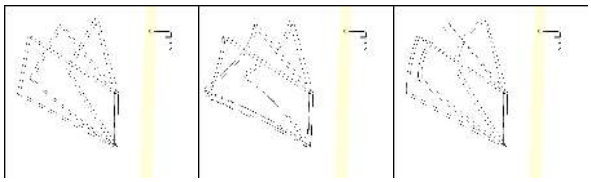

(a) (b) (c)

Figure 3: Three dimensional overview of the instrokes of the three cases. a) Rigid case; b) Deforming end case; c) Deforming center case

3.3 *Deforming center*

The second deforming case allows the leading edge to rotate. It again uses a quadratic function to describe the deformation, with this case having the maximum deformation at the center of the chord. The deformation is given by Equation 6.

$$\delta_{center} = -D_{center}^{max} \left[1 - 4\left(\frac{z}{c} - 0.5\right)^2\right] \sin(kT) \tag{6}$$

The deformation given by Equation 6 is combined with the angle of attack given by Equation 4 to give the complete deformed shape in time. The resulting cross-sectional shape of the wing is shown in Figure 2c. From the figure it is clear that for this case the deformation decreases the angle of attack at the leading edge compared to the rigid case.

In insect wings the deformation is usually higher near the wing tip due to torsional flexibility of the wing [25]. This is included in the present simulation model by varying the maximum deformation linearly along the span, resulting in a undeformed unrotated chord at the root of the plate and the maximum rotation and deformation at the tip. All deformation parameters are shown in Table 2. Three dimensional views of the instroke of the three cases are shown in Figure 3. Note in view of this spanwise deformation, that the ïrigidc̈ase indicates that there is no chordwise deformation, but it does not imply that the wing is rigid as a whole.

Parameter	Root value	Tip value
Angle α_{max}	0°	30°
D_{end}^{max}	0	0.5
D_{center}^{max}	0	0.175

Table 2: Deformation parameters.

4 RESULTS

For the three cases the lift coefficients were calculated, and averaged over the last 3 cycles. Figure 4 shows the lift coefficient C_L, as well as the cycle average value. Here C_L is

Case	Average C_L
Rigid	0.5558
Deforming center	0.6171
Deforming end	0.5948

Table 3: Cycle averaged values of C_L for the cases.

defined as $C_L = \frac{L}{1/2\rho U^2 S}$ with lift L positive in negative z-direction. Although averaging the plots over 3 cycles reduces the fluctuations which are caused by the moving boundary, they are still present to some extent. Figure 4 represent one entire cycle, starting with an outstroke. The value of the cycle average C_L for the three cases is given in Table 3. It is observed that both deforming cases produce a higher average and peak lift than the rigid case.

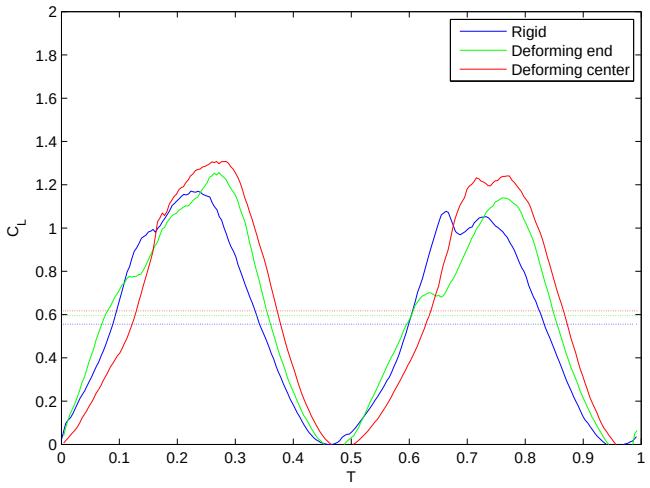

Figure 4: C_L for the three cases. The motion starts with an outstroke.

A noticeable difference between the three cases is the C_L buildup at the beginning of both the instroke and the outstroke. The deforming end case shows the fastest C_L buildup, followed by the rigid case, and the deforming center case shows the slowest buildup. The difference in C_L buildup speed is caused by different LEV buildup speeds, and is related to the difference in leading edge orientation, as can be seen from Figure 5. This figure shows the Q criterion contour plots at half of the span, at the beginning of the outstroke. The deforming end case shown in Figures 5e and 5f clearly shows that the higher angle of attack in the deforming end case creates a stronger LEV compared to the rigid case (Figures 5a and 5b). The deforming center case shown in Figures 5c and 5d has a lower angle of attack and can be seen to create a weaker LEV.

The second clear difference between the cases is the distinct dip in C_L that can be seen in Figure 4 during the acceleration phase of the plates. This dip occurs both during the out-

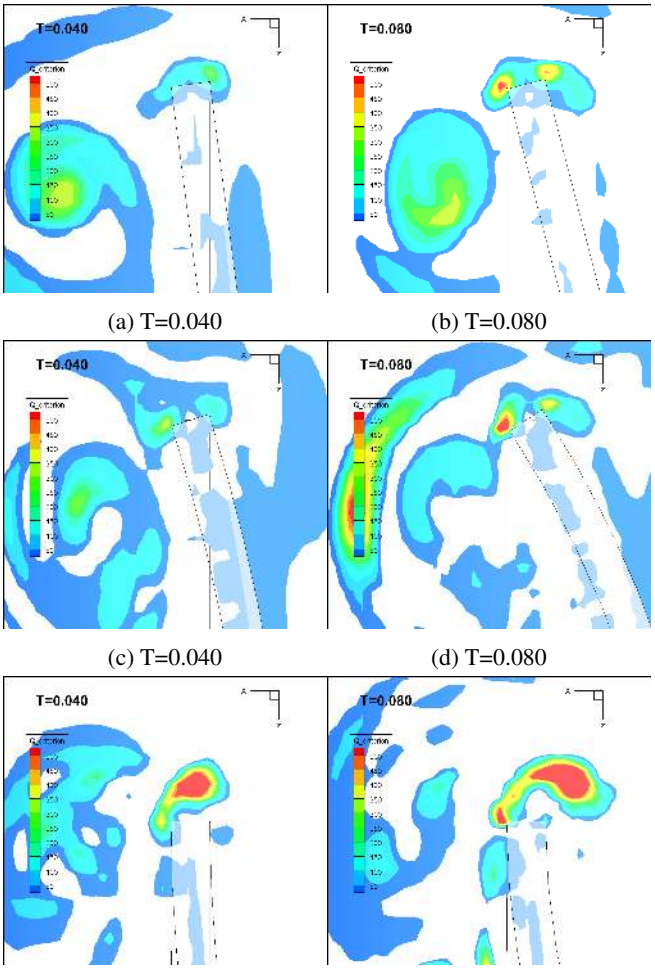

(a) T=0.040 (b) T=0.080

(c) T=0.040 (d) T=0.080

(e) T=0.040 (f) T=0.080

Figure 5: Q criterion contour plots of the three cases at the start of the outstroke with the plate moving to the left. Top: rigid case; middle: deforming center; bottom: deforming end

stroke and the instroke. The contour plots of the Q criterion are investigated at the moments around this dip during the instroke, at T=0.559, 0.599 and 0.639 at 50% of the span to see if this is associated to shedding of the LEV, to which such a decrease in lift buildup is commonly associated. The plots are shown for the deforming center and deforming end cases in Figure 6. Although it can be seen that the LEV moves further away from the plate for the deforming end case, the difference does not explain the large dip shown in C_L. Contour plots of the Q criterion at different locations along the span do not show distict shedding of the LEV either. Since the shedding of the LEV cannot be identified as the source for the dip, the pressure isosurfaces are investigated as further means to visualize the vortex behaviour around the wings. The pressure isosurfaces with $p = -1$ at the beginning of the instroke are shown in Figure 7. In Figures 7a and 7b the vortices from the previous outstroke stroke can be clearly identified, with the shed tip vortex, trailing edge vortex and LEV in front of the plate. Figure 6c show that at T=0.64, the new LEV in the deforming end case interacts with the previously shed LEV, this instant corresponds to the dip in C_L in Figure 4. The deforming center case shows no interaction, and no change in the C_L slope as seen in Figure 4. At the next instance, shown in Figure 7e the shed LEV from the previous stroke has been completly absorbed into the new LEV for the deforming end case, and C_L is again increasing. For the deforming center case the dip occurs much later, as does the interaction between the previously shed vortex and the new LEV.

From the previous results it can be concluded that not the shedding of the LEV is responsible for the dip in C_L seen in Figure 4, but the interaction of the LEV with the shed LEV from the previous stroke. For this to be true there should be no dips in the buildup of C_L during the initial stroke, since there will be no previously shed vortices in this case, and investigation shows that these dips are indeed absent [23]. The faster buildup of the LEV in the deforming end case causes the interaction with the shed vortex to occur earlier. The lowering of the angle of attack by the deforming center case delays the interaction and reduces the negative effect. The curvature of the chord of the plate in the deforming center case also causes the previously shed vortex to get trapped below the plate, delaying the interaction further. This can be clearly seen in Figure 8.

To investigate the effect of the deformation on the clap and fling mechanism the distance to the symmetry plane was varied. Three cases are defined with **D**=0.25c, 0.50c and a case without symmetry plane. Table 4 shows the increase in the average C_L compared to the case without symmetry plane, for both the rigid case and the deforming center case. Although the average C_L increases for both cases when the symmetry plane is closer an important difference can be noted. The increase in average C_L is higher for the deforming center case with the symmetry plane at **D**=0.50c, but higher for the rigid case with the symmetry plane at **D**=0.25c. The

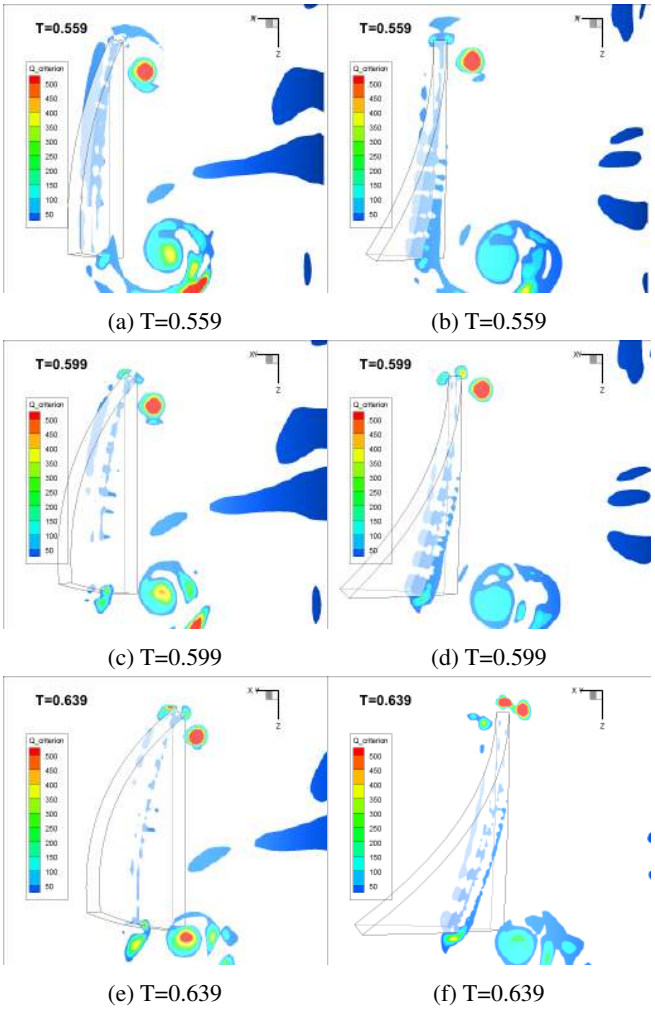

(a) T=0.559 (b) T=0.559

(c) T=0.599 (d) T=0.599

(e) T=0.639 (f) T=0.639

Figure 6: Q criterion contour plots of the deforming end and deforming center cases during the instroke, with the wings moving to the right. The deforming center case on the left and the deforming end case on the right.

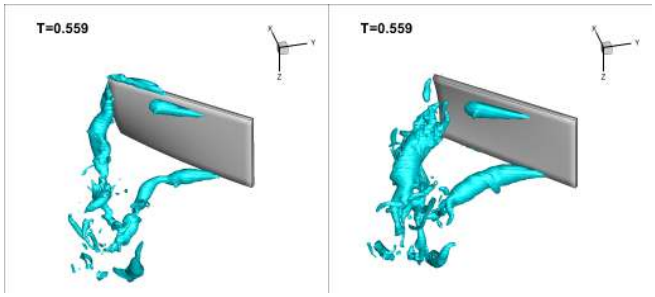

(a) T=0.559 (b) T=0.559

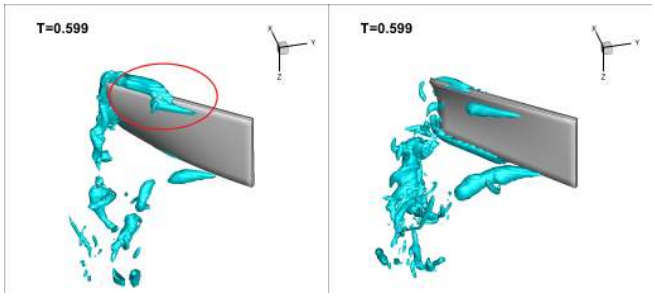

(c) T=0.599 (d) T=0.599

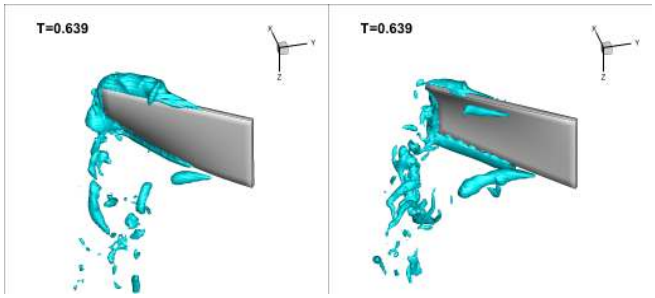

(e) T=0.639 (f) T=0.639

Figure 7: Pressure isosurfaces of $p = -1$ at the starting of the instroke with the plate moving to the front. Left for the deforming end case and right for the deforming center case.

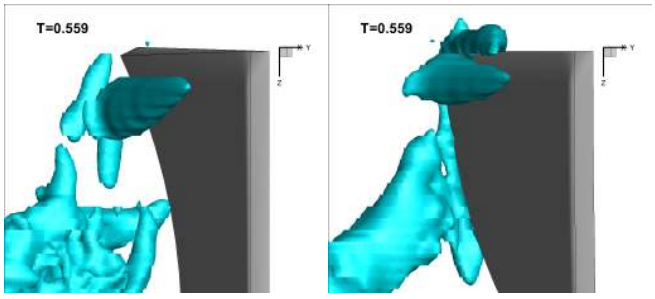

(a) Deforming center (b) Deforming end

Figure 8: Previously shed vortices at the beginning of the instroke for the the deforming center and deforming end cases.

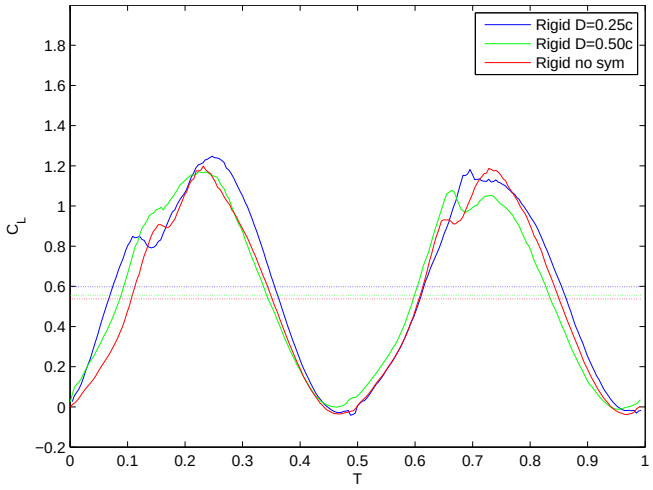

Figure 9: Lift coefficient plot for the rigid cases, at different distances from the symmetry plane. The motion starts with an outstroke.

difference between the cases can be explained by looking at the development in C_L as shown in Figures 9 and 10. Figure 10 clearly shows a very large dip in C_L buildup during the outstroke for the case with **D**=0.25c. This dip is much larger than for the case with the symmetry plane at **D**=0.50c, and greatly reduces the average C_L. The faster LEV buildup caused by the presence of the symmetry plane causes the interaction between the LEV and the previously shed vortex to occur sooner. Since the previously shed vortex is trapped below the wing as was shown in Figure 8b, the interaction takes significantly longer than for the rigid case. This longer interaction limits the benefit of fast LEV buildup.

	0.5c	0.25c
Rigid case	+3.4%	+11.3%
Deforming center case	+5.1%	+9.2%

Table 4: Increase in cycle average C_L by changing distance to symmetry plane.

5 Conclusion

Three different deforming wings were simulated to investigate the effect of the deformation on lift generation by unsteady aerodynamic mechanisms. It was shown that deforming the wing in such a way that the angle of attack near the leading edge increased, leads to faster LEV buildup and with this a faster buildup of lift. No shedding of the LEV was observed in any of the cases even when deformation caused a high angle of attack near the leading edge. The distinct dip in lift buildup that was observed was shown to be caused by the interaction between the previously shed vortex and the newly developing LEV. This interaction occurred faster when the angle of attack near the leading edge was increased, and

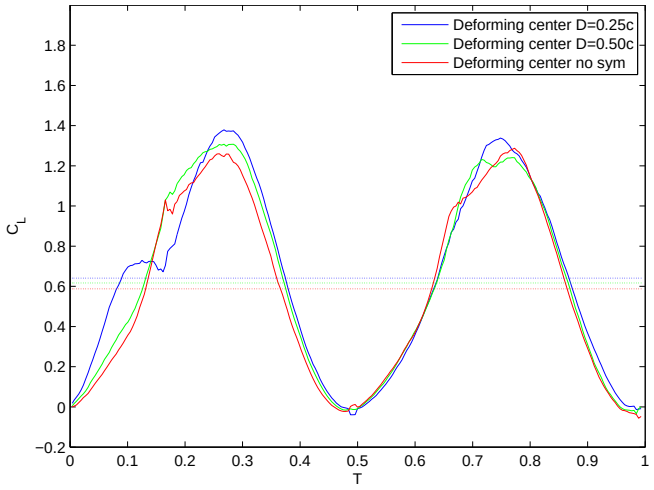

Figure 10: Lift coefficient plot for the deforming center cases, at different distances from the symmetry plane. The motion starts with an outstroke.

slower when the angle of attack was decreased. The lower angle of attack caused the previously shed vortex to get trapped below the wing preventing the interaction. Moving the wing closer to the symmetry plane had a positive effect on the cycle average value of C_L. This positive effect was reduced however by the earlier interaction between the LEV and the previously shed vortex. This was especially clear for the case were the angle of attack was reduced, since the position of the previously shed vortex caused the interaction to take longer.

References

[1] S. A. Ansari, N. Phillips, G. Stabler, P. C. Wilkins, R. Zbikowski, and K. Knowles. Experimental investigation of some aspects of insect-like flapping flight aerodynamics for application to micro air vehicles. *Experiments in Fluids*, 46:777–798, 2009.

[2] R. Zbikowski. On aerodynamic modeling of an insect-like flapping wing in hover for micro air vehicles. *Philosophical Translations of the Royal Society of London A*, 360:273–290, 2002.

[3] R. B. Srygley and A. L. R. Thomas. Unconventional lift-generating mechanisms in free-flying butterflies. *Nature*, 420:660–664, 2002.

[4] C. P. Ellington, C. van den Berg, A. P. Willmott, and A. L. R. Thomas. Leading-edge vortices in insect flight. *Nature*, 384:626–630, 1996.

[5] M. H. Dickinson, F. O. Lehmann, and S. P. Sane. Wing rotation and the aerodynamic basis of insect flight. *Science*, 284, 1999.

[6] F.-O. Lehmann and S. Pick. The aerodynamic benefit of wing-wing interaction depends on stroke trajectory in flapping insect wings. *The Journal of Experimental Biology*, 210:1362–1377, 2007.

[7] L. David, T. Jardin, P. Braud, and A. Farcy. Time-resolved scanning tomography piv measurements around a flapping wing. *Experiments in Fluids*, 52:857–864, 2012.

[8] D. Kim, F. Hussain, and M. Gharib. Vortex dynamics of clapping plates. *The Journal of Fluid Mechanincs*, 714:5–23, 2013.

[9] Z. Wang. Two dimensional mechanism for insect hovering. *Physical Review letters*, 85(10):2216–2219, 2000.

[10] B. Yin and H. Luo. Effect of wing inertia on hovering performance of flexible flapping wings. *Physics of Fluids*, 22(11):1071–1080, 2010.

[11] J. D. Eldredge, J. T., and A. Medina. On the roles of chordwise flexibility in a flapping wing with hovering kinematics. *Journal of Fluid Mechanics*, 659:94–115, 2010.

[12] T. Gillebaart. Influence of flexibility on the clap and peel movement of the DelFly II. Master's thesis, Delft University of Technology, 2011.

[13] J. R. Usherwood and C. P. Ellington. The aerodynamics of revolving wings I. model hawkmoth wings. *The Journal of Experimental Biology*, 205:1547–1564, 2002.

[14] J. A. Walker. Rotational lift: something different or more of the same? *The Journal of Experimental Biology*, 205:3783–3792, 2002.

[15] T. Jardin, A. Farcy, and L. David. Three-dimensional effects in hovering flapping flight. *The Journal of Fluid Mechanics*, 702:102–125, 2012.

[16] P. Trizila, C.K. Kang, H. Aono, and W. Shyy. Low-reynolds-number aerodynamics of a flapping rigid flat plate. *AIAA Journal*, 49(4):806–824, 2011.

[17] K. M. E. de Clercq, R. de Kat, B. Remes, B. W. van Oudheusden, and H. Bijl. Aerodynamic experiments on delfly II: Unsteady lift enhancement. *International Journal of Micro Air Vehicles*, 1(4):217–224, 2009.

[18] E. A. Fadlun, R. Verzicco, P. Orlandi, and J. Mohd-Yusof. Combined immersed-boundary finite-difference methods for three-dimensional complex flow simulations. *Journal of Computational Physics*, 161:35–60, 2000.

[19] J. Kim, D. Kim, and H. Choi. An immersed-boundary finite-volume method for simulations of flow in complex geometries. *Journal of Computational Physics*, 171:132–150, 2001.

[20] J. Yang and E. Balaras. An embedded-boundary formulation for large-eddy simulation of turbulent flows interacting with moving boundaries. *Journal of Computational Science*, 215:12–40, 2006.

[21] C. C. Liao, Y. W. Chang, C. A. Lin, and J.M. McDonough. Simulating flows with moving rigid boundary using immersed-boundary method. *Computers & Fluids*, 39:152–167, 2010.

[22] W.B. Tay, B. W. van Oudheusden, and H. Bijl. Numerical simulation of x-wing type biplane flapping wings in 3d using the immersed boundary method. *Bioinspiration and Biomimetics*, 9:1–21, 2014.

[23] T. A. Noyon. The effect of wing deformation on the unsteady aerodynamic mechanisms in hovering flapping flight. Master's thesis, Delft University of Technology, 2014.

[24] R. Dudley. *The Biomechanics of Insect Flight: Form, Function, Evolution*. Princeton University Press, reprint edition, 2002.

[25] K. Mazaheri and A. Ebrahimi. Experimental investigation of the effect of chordwise flexibility on the aerodynamics of flapping wings in hovering flight. *Journal of Fluids and Structures*, 26:544–558, 2010.